

Synthesis, structure and luminescence of Er³⁺-doped Y₃Ga₅O₁₂ nano-garnetsVemula Venkatramu,^a Sergio F. León-Luis,^b Ulises R. Rodríguez-Mendoza,^b Virginia Monteseuro,^b Francisco J. Manjón,^c Antonio D. Lozano-Gorrín,^d Rafael Valiente,^e Daniel Navarro-Urrios,^f C. K. Jayasankar,^g Alfonso Muñoz^d and Víctor Lavín^{*b}

Received 6th March 2012, Accepted 1st May 2012

DOI: 10.1039/c2jm31386c

A novel Y_{3(1-x)}Er_{3x}Ga₅O₁₂ nanocrystalline garnet has been synthesized by a sol-gel technique and a complete structural, morphological, vibrational, and optical characterization has been carried out in order to correlate the local structure of the Er³⁺ ions with their optical properties. The synthesized nanocrystals are found in a single-phase garnet structure with an average grain size of around 60 nm. The good crystalline quality of the garnet structure is confirmed by FTIR and Raman measurements, since the phonon modes of the nano-garnet are similar to those found in the single crystal garnet. Under blue laser excitation, intense green and red visible and 1.5 μm infrared luminescences are observed, whose relative intensities are very sensitive to the Er³⁺ concentration. The dynamics of these emissions under pulsed laser excitations are analyzed in the framework of different energy transfer interactions. Intense visible upconverted luminescence can be clearly observed by the naked eye for all synthesized Er³⁺-doped Y₃Ga₅O₁₂ nano-garnets under a cw 790 nm laser excitation. The power dependency and the dynamics of the upconverted luminescence confirm the existence of different two-photon upconversion processes for the green and red emissions that strongly depend on the Er³⁺ concentration, showing the potential of these nano-garnets as excellent candidates for developing new optical devices.

A Introduction

Nowadays, rare earth (RE³⁺)-doped nanocrystals attract great attention due to their size, shape, and phase-dependent structural and luminescence properties, which make them suitable for fundamental and technological applications.^{1,2} On the other hand, the favorable physical and chemical properties of the oxide garnet crystals, such as high transparency from the UV to the mid-IR, high thermal conductivity, hardness, good chemical stability, and relatively low-energy phonons, make them one of the most important families of host matrices for the RE³⁺ ions with interesting luminescence properties already used in lasers

and phosphors.¹ In fact, the Nd³⁺-doped Y₃Al₅O₁₂ (YAG) garnet is one of the most well-known and used laser-active materials.

In the last decade, large efforts have been made to investigate the luminescence properties of RE³⁺-doped nanostructured garnets,³⁻⁵ especially in the development of lasers and phosphors in lightning applications, 3-D optical imaging for displays and as an alternative to quantum dots in the development of photonic and optoelectronic devices. The Y₃Al₅O₁₂ (YAG)^{6,7} and the Gd₃Ga₅O₁₂ (GGG) nanostructures have proved to be efficient, flexible and robust luminescent materials and can support high concentrations of RE³⁺ ions through substitution of Y³⁺ or Gd³⁺ ions without charge compensation.^{8,9}

From the point of view of the potential optical applications of the RE³⁺ ions, one of the most interesting phenomena is their capacity to convert the infrared absorbed radiation into visible emitting light, known as energy upconversion.¹⁰ The particular selection of one or various RE³⁺ ions and their concentrations allows controlling the upconverted visible luminescence to match a specific coordinate of colour, or even the generation of white light as a combination of red, green and blue (RGB) emissions. Thus there is an increasing demand for upconversion materials with important applications in upconversion lasers, due to the availability of powerful near-infrared commercial laser diodes, IR detection by conversion to visible light, where detectors are more efficient, and biological fluorescence labels and imaging or 3-D displays.^{1,2,11-16} When the RE³⁺ ions are incorporated into the nanocrystals their upconversion efficiencies depend on the

^aDepartment of Physics, Yogi Vemana University, Kadapa 516 003, India^bDepartamento de Física Fundamental y Experimental, Electrónica y Sistemas and MALTA Consolider Team, Universidad de La Laguna, 38200 San Cristóbal de La Laguna, Santa Cruz de Tenerife, Spain. E-mail: vlavin@ull.edu.es; Fax: +34 922318228; Tel: +34 922318321^cInstituto de Diseño para la Fabricación y Producción Automatizada and MALTA Consolider Team, Universitat Politècnica de València, 46022 València, Spain^dDepartamento de Física Fundamental II and MALTA Consolider Team, Universidad de La Laguna, 38200 San Cristóbal de La Laguna, Santa Cruz de Tenerife, Spain^eDepartamento de Física Aplicada and MALTA Consolider Team, Universidad de Cantabria, 39005 Santander, Cantabria, Spain^fCatalan Institute of Nanotechnology (CIN2-CSIC), Campus UAB, Edifici CM3, 08193 Bellaterra, Spain^gDepartment of Physics, Sri Venkateswara University, Tirupati 517 502, Andhra Pradesh, India

RE³⁺ ion concentration, the size of the nanocrystals, the intra- or inter-particle energy transfer processes, and the rate of the multiphonon relaxation.^{1,2,16} Hence, there is a need for a rigorous search for RE³⁺-doped hosts with low-energy phonons, high quantum efficiencies, and optimized nanocrystal size and RE³⁺ concentrations in order to have the most efficient luminescence properties.

Among the trivalent RE³⁺ ions, the erbium (Er³⁺) ion is a versatile optically active ion for upconversion since its energy-level structure contains several metastable multiplets.¹⁷ Further, it provides interesting laser emissions at around 1.5 μm , associated with the $^4\text{I}_{13/2} \rightarrow ^4\text{I}_{15/2}$ transition and widely used in optical telecommunication and range-finding applications, and at around 2.9 μm , associated with the $^4\text{I}_{11/2} \rightarrow ^4\text{I}_{13/2}$ transition used in medical applications. Moreover, an efficient upconversion laser in the visible region pumped by an infrared laser diode has been obtained with a higher efficiency than that achieved by second harmonic generation techniques due to broad pumping mechanisms.^{18–20}

This work presents for the first time, as far as we know, the synthesis of Er³⁺-doped Y₃Ga₅O₁₂ (YGG) nano-garnet using an easy citrate sol–gel method, as well as the study of the correlation between the nanocrystal structure and morphology and the Stokes and upconverted luminescence properties. This characterization was carried out as a function of the concentration of the optically active ion in order to carefully control the Er³⁺ luminescence in the nano-garnet.

B Experimental

Nanocrystalline yttrium gallium garnets of composition Y_{3(1-x)}Er_{3x}Ga₅O₁₂, with $x = 0.01, 0.05$ and 0.1 and hereafter called YGG1Er, YGG5Er and YGG10Er, were successfully synthesized by the citrate sol–gel method in an air atmosphere.²¹ Stoichiometric molar ratios of high-purity Ga(NO₃)₃·9H₂O, Y(NO₃)₃·4H₂O and Er(NO₃)₃·5H₂O materials were dissolved in 25 ml of 1 M HNO₃ under stirring at 353 K for 3 h. Then citric acid, with a molar ratio of metal ions to citric acid of 1 : 2, was added to the solution, which was stirred for a further 2 h and finally dried at 363 K for 36 h. This process created a gel that was fired at 773 K for 4 h in order to remove the residual nitrates and organic compounds and the subsequently obtained powder sample was finally calcined at 1173 K for 16 h.

The HRTEM micrographs (FEI-TECNAI G2 microscope at 200 kV) were used to study the morphology and the nanostructure of the YGG powder. The X-ray diffraction patterns of the YGG nano-garnets were measured using the CuK _{α} 1 (1.5406 Å) radiation in the range of $2\theta = 10\text{--}80^\circ$, with a step size of 0.02° (PANalytical X'Pert Pro). The infrared absorption spectrum was recorded using a FTIR spectrometer (Bruker IFS66), whereas the Raman spectrum was obtained in back-scattering geometry (Horiba Jobin Yvon LabRAM HR UV) with resolution better than 2 cm^{-1} and exciting with the unfocused 632.8 nm radiation of a 30 mW He–Ne laser.

The visible and NIR diffuse reflectance spectrum in the range from 200 to 1800 nm was measured using an integrating sphere with a Cary 6000i (Varian). The luminescences of the Er³⁺-doped YGG nano-garnet powders were measured by exciting at 488 nm using the laser line of an Ar⁺ laser (2060-10 Beamlock Spectra

Physics) for the visible range or at 790 nm using a Ti:sapphire laser (3900S Spectra Physics) pumped by the Ar⁺ laser for the NIR range. These emissions were focused with a convergent lens onto a 0.75 m single-grating monochromator (Jobin Yvon Spex750M) with a resolution of 0.1 nm and then detected either with a photomultiplier tube (Hamamatsu R928) or an InGaAs detector. Moreover, under a cw 790 nm laser excitation, the green and red upconverted luminescences were focused with a convergent lens onto a fiber coupled 0.303 m single-grating spectrograph (Andor Shamrock SR-303i-B) and detected with a cooled CCD detector (Newton DU920N). The luminescence decay curves and the dynamics of the upconverted emissions were measured by exciting the Er³⁺ ions with a 10 ns pulsed optical parametric oscillator OPO (EKSP/LA/NT342/3/UVE) using a digital storage oscilloscope (LeCroy WS424) coupled to the detection system. All spectra were corrected for the spectral response of the equipment.

C Results and discussion

C.1 Morphological and structural properties

The HRTEM micrographs of the synthesized powder obtained, shown in Fig. 1, reveal that nanocrystalline powder has been obtained in the form of agglomerated nanocrystals in different shapes with different sizes ranging from 40 to 60 nm. The existence of aggregated particles has been ascribed to the bridging of adjacent particles through the hydrogen bonding of water and the significant capillary action generated during the drying process in the precursors.²² HRTEM images show that the lattice spacing between different layers of Er³⁺-doped nanoparticles is around 4.60 Å, which corresponds to the (220) plane of the cubic phase of the YGG nano-garnets. The distance between the layers corresponding to the (220) plane in bulk YGG is 4.34 Å, which is smaller than the distance obtained for the nanocrystal. Thus, from the HRTEM pictures it can be concluded that an increase in the lattice parameter of the nanoparticles is accompanied by a decrease in their sizes.

X-ray diffraction measurements reveal well-defined Bragg reflections of the nanocrystalline powder samples, indicating that the material under study is well-crystallized in a single phase of cubic crystalline structure,²³ without appreciable changes due to the Er³⁺ doping concentration (see Fig. 2 for the YGG1Er nano-garnet). These patterns have been indexed to the Y₃Ga₅O₁₂ (YGG) garnet structure with an $Ia\bar{3}d$ (no. 230) space group and refined by both the Le Bail and the Rietveld method²⁴ using the FULLPROF program.²⁵ The Le Bail fitting allows getting more accurate values of the shape and cell parameters in terms of profile matching, being a reliable first step before carrying out the Rietveld fitting, since it gives more accurate results for both the shape and the lattice as starting values for the refinement. The Rietveld fitting, carried out after adding the atomic positions to the Le Bail output, has been done by the refinement of 21 parameters, a pseudo-Voigt profile function, and a polynomial function with six refinable coefficients for the background. The cell parameters and the reliability factors for both fittings are summarized in Table 1. The fittings are quite good and only small differences have been found for the amplitudes of a few peaks, as can be observed in Fig. 2 for the Le Bail refinement. The average

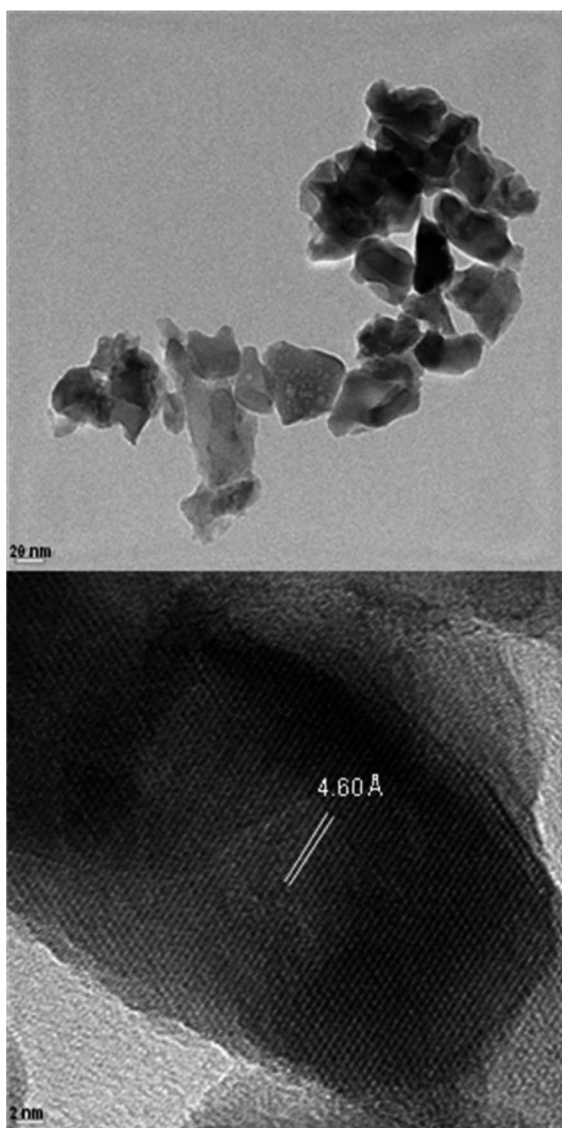


Fig. 1 High resolution transmission electron microscope (HRTEM) micrographs of the YGG nano-garnets.

crystallite size has been estimated to be around 60 nm for the three samples under study from the full width at half maximum (FWHM) of the diffraction peak at 32.71° using the Scherrer equation along with the structure of the YGG unit cell,²⁶ confirming the estimations made using the HRTEM micrographs.

The YGG garnet crystal structure can be described as a network of GaO_6 octahedra and GaO_4 tetrahedra linked by shared oxygen ions at the corners of the polyhedra (see Fig. 2). These polyhedra are arranged in chains along the three crystallographic directions and form dodecahedral cavities which are occupied by the Y^{3+} ions. Thus the YGG garnet possesses three crystallographically distinct cation sites,²⁷ i.e., the Ga^{3+} ions are located both in 24(d) tetrahedral S_4 sites and 16(a) octahedral S_6 sites with fourfold and sixfold coordination, respectively, while the Y^{3+} ions are located in a 24(c) dodecahedral D_2 site with a coordination number of 8. The O^{2-} ions occupy the 96(h) sites with each one being a member of one tetrahedron, one octahedron, and two dodecahedra. Due to ionic size considerations in

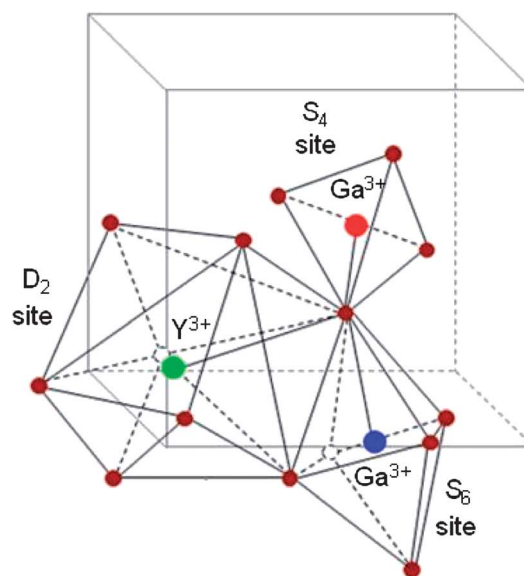
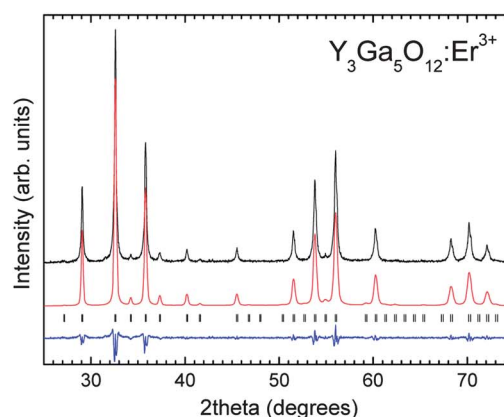


Fig. 2 (Top) X-ray diffraction pattern (upper) and Le Bail refinement (lower) of the YGG1Er nano-garnet. The lower part of the figure shows the difference between the observed and the calculated plots and the vertical marks are the allowed reflections for this material in the $Ia\bar{3}d$ (no. 230) space group. (Bottom) unit cell of the YGG crystal, where the spheres show the position of the Y^{3+} ions occupying a D_2 point symmetry site and the S_4 and S_6 site positions of the Ga^{3+} ions.

Table 1 Cell parameters and reliability factors obtained from the Le Bail and the Rietveld refinements

a (Å)	V (Å ³)	χ^2	R_p	R_{wp}	R_{exp}
<i>Le Bail fitting</i>					
12.2833(3)	1853.296	5.00	7.87	10.3	4.62
<i>Rietveld fitting</i>					
12.2816(5)	1852.528	14.5	13.0	17.8	4.69

the YGG lattice, the RE^{3+} ions are expected to predominantly enter into the distorted dodecahedral sites by replacing the Y^{3+} ions and to be coordinated to eight O^{2-} ions.²⁸

The vibrational modes of the different polyhedra of YGG can be studied by FTIR and Raman spectroscopy.²⁹ The FTIR spectrum of the YGG nano-garnet powder, shown in Fig. 3,

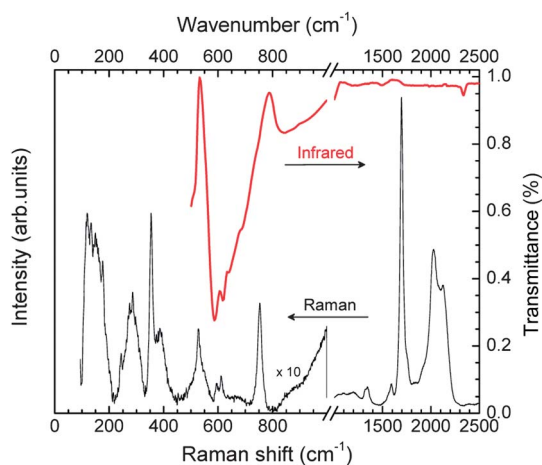


Fig. 3 FTIR and Raman spectra of the YGG nano-garnets.

consists of two main bands with superimposed peaks whose energies range from 520 to 1100 cm^{-1} , in addition to different broad peaks at higher energies. The peaks with maxima at around 590, 620, 640, 685 and 840 cm^{-1} correspond to the formation of the nanocrystalline YGG and are assigned to the characteristic metal–oxygen stretching vibrational modes of the GaO_4 tetrahedra in the garnet structure.^{23,30}

The Raman spectrum of the YGG nano-garnets has been measured in the 100–2500 cm^{-1} range and the observed modes are summarized in Table 2. The primitive cell of a garnet lattice contains four formula units (80 atoms)³¹ in which, from a factor group analysis, there are 25 Raman-active modes that can be classified as 3 A_{1g} , 8 E_g and 14 T_{2g} modes.³² It is worth noting that out of 25 predicted Raman-active modes, 17 of them are experimentally observed for nanocrystalline YGG and are compared with vibrational modes of YGG single crystals²⁹ (see Table 2). A quite good agreement is observed between the vibrational modes of the nano-YGG and the YGG single-crystal and, in general, only slight shifts in frequency have been found between the Raman modes of nanocrystals and those of the bulk

Table 2 Comparison of the energies of the experimental Raman vibrational modes (in cm^{-1}) of the YGG nano-garnets and single crystal

Vibrational phonon mode	YGG nano-garnet (present work)	YGG single crystal (ref. 29)
T_{2g}	119	119 (theory)
E_g	133	134
T_{2g}	151	155 (theory)
T_{2g}	175	176
T_{2g}	187	180
T_{2g}	243	243
T_{2g}	272	274
E_g	286	287
E_g	300	324
A_{1g}	357	356
T_{2g}	393	392
E_g	411	412
T_{2g}	420	432
A_{1g}	528	529
T_{2g}	594	596
T_{2g}	612	611
E_g	—	635
T_{2g}	752	754

material, and these are within the accuracy limits of the measurements.

The Raman spectrum of garnets has been interpreted on the basis of the vibrational modes of the tetrahedral GaO_4 and octahedral GaO_6 units, considering that the vibrations of the different polyhedra are strongly coupled to each other.^{33,34} While the assignment of the different Raman modes to the different vibrations in terms of eigenmodes is very clear in the $\text{Y}_3\text{Al}_5\text{O}_{12}$ (YAG) crystal,³⁵ the same situation is not so evident in the $\text{Y}_3\text{Ga}_5\text{O}_{12}$ (YGG) crystal.²⁹ The Raman spectrum of YGG can be divided into two main regions: the low-frequency region (100–340 cm^{-1}) and the high-frequency region (340–800 cm^{-1}). Starting with the latter and according to Saine *et al.* (1982),³⁴ the bands comprised in the 340–450 cm^{-1} and the 580–700 cm^{-1} ranges can be attributed to the antisymmetric stretching modes of the GaO_6 and GaO_4 polyhedra, respectively. However, the band at 360 cm^{-1} can be assigned to the symmetric stretching mode of the GaO_4 tetrahedron coupled with a rotational mode involving the whole tetrahedron. Finally, the band observed at around 760 cm^{-1} is mainly due to the symmetric stretching mode of the GaO_4 tetrahedron, even if a weaker contribution due to the antisymmetric stretching mode of the same polyhedron could be present.³⁴

The bands in the low energy region are mainly due to the O–Ga–O bending modes of the Ga-related polyhedra and to lattice modes related to the movements of the Ga-related polyhedra against the Y^{3+} ions, which can also be considered as stretching or bending modes of the YO_8 dodecahedra. In this sense, it is important to note that the stretching and bending forces of Y^{3+} ions in YO_8 dodecahedra are considerably smaller than those of GaO_4 tetrahedra and similar to those of GaO_6 octahedra in garnets.²⁹ In particular, the two lowest-energy E_g phonons at 133 and 286 cm^{-1} have frequencies that exhibit a strong dependence on the lattice parameter and correspondingly on the RE^{3+} mass, being the smallest in frequency attributed to the translation of YO_8 units. On the other hand, the T_{2g} modes at 187 and 272 cm^{-1} have been shown to be almost volume-independent and this behavior could be related to canceling contributions due to the intermixing of octahedral and dodecahedral molecular modes.²⁹ Therefore, all these low-frequency E_g and T_{2g} modes could yield important information regarding the occupation of the dodecahedral sites by the Er^{3+} ions. In fact, since this is a low-energy phonon site, the multiphonon relaxation probabilities in the YGG nano-garnets may be considered one of the lowest found in oxide matrices, and could yield high quantum efficiencies for the emitting levels of the Er^{3+} ions.

Despite the measured FTIR and Raman spectra confirming the good crystalline quality of these nanocrystals of garnet structure, there are a few Raman and IR peaks above 1100 cm^{-1} whose explanation is not easy, although it is accepted that their presence is related to the anions attached to the nano-garnet crystal surface during the synthesis process. In principle, the presence of these anionic groups on the nanoparticles surface is potentially undesirable since they may act as quenching traps, diminishing the luminescence and lifetimes of the RE^{3+} emitting levels. The peak at around 1500 cm^{-1} could be assigned to CO_3^{2-} carbonate groups, while the bands in the range from 2000 to 2350 cm^{-1} could arise from the carbon dioxide in air. Finally,

another band at around 3550 cm^{-1} (not shown) is associated with the OH^- anionic groups arising from the water adsorbed during the exposure of dried powder to air. The presence of high energy vibrations may indicate that the heat treatment was not enough to remove either the carbonate or the hydroxyl ions from the nanocrystal surface, since these bands have been shown to disappear after synthesis at a higher temperature.²³

C.2 Absorption and luminescence

For optical applications special interest is devoted to the analysis of the local structure around the RE^{3+} ions in the matrix, since it rules the fine structure splitting of the free-ion multiplets and the forced intra-configurational $4f-4f$ electric-dipole transition probabilities in the visible range. The optical properties of the RE^{3+} ions and, therefore, their interest for optical applications depend on the final environment of these ions.³⁶

As already mentioned, the Er^{3+} ions will predominantly enter the distorted dodecahedral sites by replacing the Y^{3+} ions. Thus the eight oxygen ligands surrounding the optically active Er^{3+} ion create a local environment with orthorhombic D_2 point symmetry. As a consequence, the D_2 crystal-field interaction felt by the optically active ion will completely remove the degeneracy of the $2^{5+1}L_J$ multiplets of the free- Er^{3+} ion, giving rise to $(2J + 1)/2$ Stark, or crystal-field, levels labeled according to the irreducible representations obtained from group theory.³⁶

The room temperature (RT) diffuse reflectance spectrum of the YGG5Er nano-garnet in the UV-visible-NIR range is given in Fig. 4. The peaks observed correspond to intra-configurational $4f^{11}-4f^{11}$ electronic transitions starting from the $^4I_{15/2}$ ground state to the different excited levels of the Er^{3+} ion. All the transitions are assumed to be electric dipole in nature, except for that to the $^4I_{13/2}$ first excited state that shows a magnetic dipole contribution.³⁷ The labels of the different transitions of the Er^{3+} ion in the YGG nano-garnet have been assigned according to the well-known Dieke's diagram for this ion in the LaCl_3 crystal³⁸ and the energies of the Stark levels of Er^{3+} in a YGG single crystal summarized by Morrison and Leavitt.³⁹ A partial energy level diagram of the Er^{3+} ion in the YGG nano-garnet is given in Fig. 5. The sharp peak profiles found for all the electronic

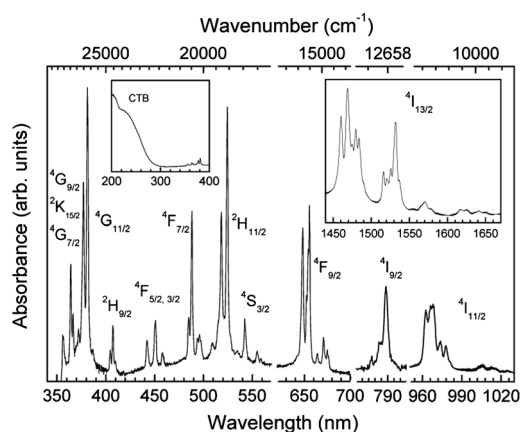


Fig. 4 Diffuse reflectance spectrum of the YGG5Er nano-garnet powder in the UV-visible-NIR range at RT. All transitions start from the $^4I_{15/2}$ ground state to the indicated levels.

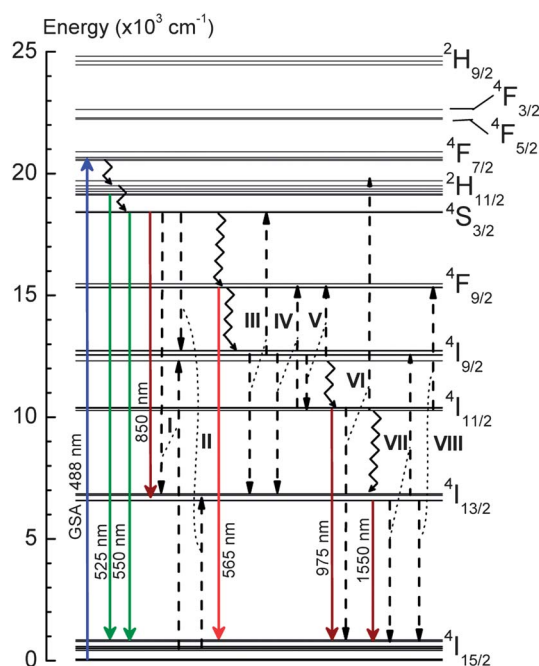


Fig. 5 Partial energy level diagram of the Er^{3+} ion showing different radiative transitions (downward solid lines) related to the luminescence after a $^4I_{15/2} \rightarrow ^4F_{7/2}$ ground state absorption (GSA) under a direct laser excitation at 488 nm. The multiphonon (zig-zag lines) and energy transfer (dashed lines) non-radiative relaxation processes are also shown.

transitions confirms that the Er^{3+} ions are incorporated in the nanocrystalline structure of the garnet. From these data, and the emission bands presented later, it can be stated that the absorption transitions at RT start mainly from the four Stark levels of the $^4I_{15/2}$ ground state with lowest energies, which are separated around 350 cm^{-1} from the Stark levels with higher energies. The intense band at around 240 nm , strongly overlapped with the absorbance of the YGG matrix, can be assigned to the $\text{Er}^{3+}-\text{O}^{2-}$ charge transfer state, although different $4f^{11} \rightarrow 4f^{10}5d$ inter-configurational transition bands of the Er^{3+} ion have also been observed in this range.⁴⁰

When the Er^{3+} ions are resonantly excited to the $^4F_{7/2}$ level with a cw 488 nm blue laser radiation, the luminescent $^2H_{11/2}$ and $^4S_{3/2}$ thermalized levels are immediately populated through non-radiative multiphonon relaxation processes and green, red, and NIR luminescence are measured (see Fig. 6). However, these emissions not only start from the $^2H_{11/2}$ and $^4S_{3/2}$ thermalized levels but also from the $^4F_{9/2}$, $^4I_{11/2}$, and $^4I_{13/2}$ multiplets populated through different non-radiative de-excitations. The only non-emitting level is the $^4I_{9/2}$ one, from which the expected emissions at around 800 and 1700 nm are not observed, even under a direct excitation of the Er^{3+} ions to this level. The emission bands are assigned in Fig. 6 and their sharp peak profiles further confirm that the Er^{3+} ions are incorporated in the YGG nano-crystals. Similar observations are found for Er^{3+} -doped $\text{Lu}_3\text{Ga}_5\text{O}_{12}$ (LuGG)³ and $\text{Gd}_3\text{Ga}_5\text{O}_{12}$ (GGG) nanocrystals⁵ and single crystals.⁴¹

Of special interest are the emission bands from the $^4I_{13/2}$ multiplet at around $1.5\text{ }\mu\text{m}$ shown in Fig. 6. The peak positions and spectral profiles of these bands are similar to those in the absorption spectrum, although their relative intensities strongly

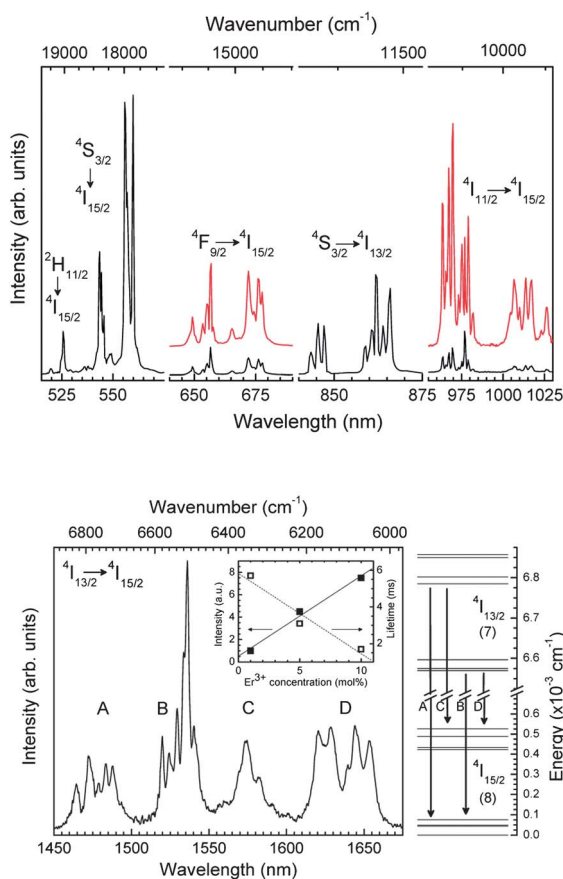


Fig. 6 (Top) Luminescence spectra of the YGG1Er and YGG10Er (overimposed) nano-garnets in the visible-NIR range at RT. The spectra are normalized to the intensity of the $^2\text{H}_{11/2}, ^4\text{S}_{3/2} \rightarrow ^4\text{I}_{15/2}$ green emission. (Bottom) $1.5 \mu\text{m}$ $^4\text{I}_{13/2} \rightarrow ^4\text{I}_{15/2}$ NIR luminescence of the YGG1Er nano-garnet. The different bands are correlated to transitions between the $^4\text{I}_{13/2}$ and $^4\text{I}_{15/2}$ Stark levels. The degeneracies of the ground and the first excited multiplets are given in parenthesis. The inset figure shows the relative intensities of the $^4\text{I}_{13/2} \rightarrow ^4\text{I}_{15/2}$ emission and the lifetime of the $^4\text{I}_{13/2}$ level as a function of the Er^{3+} concentration.

differ. The fact that the ground and the first excited multiplets of the Er^{3+} ion in the garnet crystal show a particular Stark splitting with two groups of levels separated by a few hundred cm^{-1} give rise to four bands with a rich structure of peaks between the different Stark levels. The identification of these bands is given in Fig. 6.

The dependence of the luminescence with the Er^{3+} concentration for the $^4\text{F}_{9/2}$, $^4\text{I}_{11/2}$ and $^4\text{I}_{13/2}$ emitting levels are clearly observed around 660, 975 and 1500 nm, and the emissions starting from the first two levels in the YGG10Er nano-garnet are included in red in Fig. 6 for comparison. The relative intensity of the weak $^4\text{F}_{9/2} \rightarrow ^4\text{I}_{15/2}$ red emission between 645 and 680 nm compared to the green one increases by a factor of around 4.5 when the concentration of Er^{3+} ions increases from 1 to 10 mol%. This factor is around 11 for the $^4\text{I}_{11/2} \rightarrow ^4\text{I}_{15/2}$ NIR emission at 975 nm and 7.5 for the $^4\text{I}_{13/2} \rightarrow ^4\text{I}_{15/2}$ NIR emission at $1.5 \mu\text{m}$, as shown in the inset of Fig. 6. The enhancement of these emissions with the increase of the Er^{3+} ion concentration can be ascribed to different cross-relaxation processes involving the ground state and the emitting levels.

In order to check the existence of these energy transfer channels in the YGG nano-garnets, the lifetimes of the emitting levels were measured for the YGG1Er, YGG5Er and YGG10Er nano-garnets and are reported in Fig. 7. It is known that at very low concentrations of the optically active ions, for which the interactions between them are negligible, the decay of the luminescence can be described by a single exponential. However, at higher concentrations the active ions are closer to each other and the energy transfer processes become more efficient, causing a non-exponential decay.⁴² For this reason, an effective lifetime (τ_{eff}) can be evaluated by using the following equation^{3,5}

$$\tau_{\text{eff}} = \frac{\int t \cdot I(t) \cdot dt}{\int I(t) \cdot dt} \quad (1)$$

that for the samples with higher Er^{3+} concentrations probabilities, in the presence of energy transfer processes, can be expressed as

$$\frac{1}{\tau_{\text{eff}}} = \frac{1}{\tau_0} + W_{\text{ET}} \quad (2)$$

where W_{ET} is the energy transfer probability and τ_0 is the intrinsic lifetime of the thermalized levels, involving radiative and non-radiative multiphonon de-excitation probabilities, and

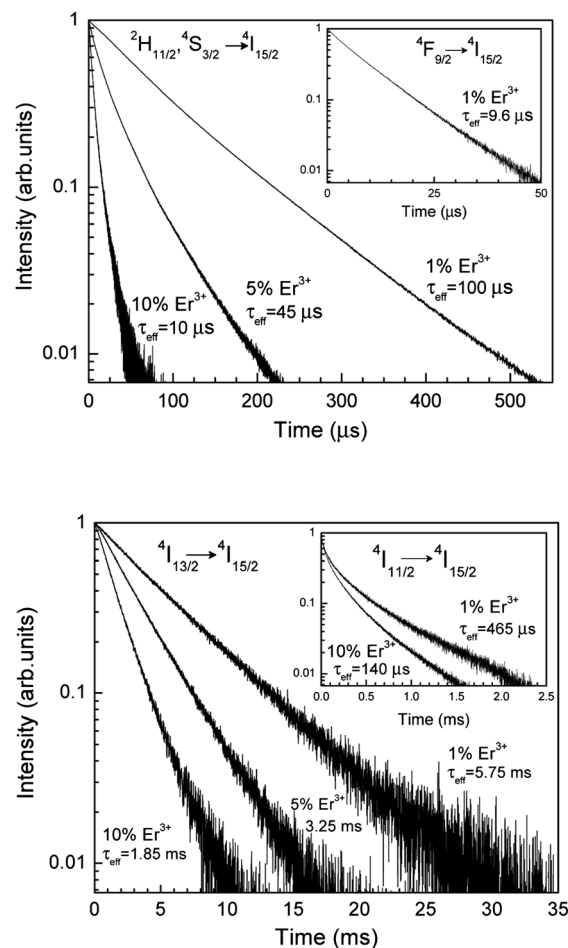


Fig. 7 Er^{3+} luminescence decay curves of the (top) green, red and (bottom) NIR emissions in YGG1Er, YGG5Er and YGG10Er nano-garnets at RT under resonant laser excitations.

can be measured if the concentration of Er^{3+} ions is low enough to neglect ion–ion interaction and, therefore, the energy transfer probabilities.

Two different temporal regimes can be observed in the YGG nano-garnets according to the order of magnitude of the lifetimes of the four emitting levels of the Er^{3+} ions. On one hand, those from the ${}^2\text{H}_{11/2}$, ${}^4\text{S}_{3/2}$, and the ${}^4\text{F}_{9/2}$ levels with typical lifetimes of the order of tens of microseconds and, on the other hand, those of the ${}^4\text{I}_{11/2}$ and ${}^4\text{I}_{13/2}$ metastable levels with longer lifetimes of hundreds or thousands of microseconds. Moreover, different dynamics are found for each emitting level.

Under resonant laser excitation at 525 nm, the τ_{eff} at RT of the ${}^2\text{H}_{11/2}$ and ${}^4\text{S}_{3/2}$ thermalized levels is found to be around 100, 45, and 10 μs for the YGG1Er, YGG5Er, and YGG10Er nano-garnets, respectively (see Fig. 7). The green luminescence decay curve for the lowest Er^{3+} concentration is quasi-exponential, indicating a homogeneous distribution and therefore an Er^{3+} – Er^{3+} distance large enough to, in a first approximation, neglect the energy transfer processes. Its effective value of around 100 μs is lower than the 125 μs found in Er^{3+} -doped GGG nanocrystals with the same concentration,⁵ probably due to differences in the multiphonon probabilities for both matrices and indicating a slightly higher radiative transition probability of the Er^{3+} ion in the YGG nano-garnet. At higher Er^{3+} concentrations, the observed non-exponential nature of the luminescence decays is accompanied by a shortening of the lifetime that is related to energy transfer processes between Er^{3+} ions and/or to different quenching traps (impurities and/or defective sites).⁴ The resonant cross-relaxation channels that depopulate these thermalized levels are the (${}^4\text{S}_{3/2}$, ${}^4\text{I}_{15/2} \rightarrow {}^4\text{I}_{13/2}$, ${}^4\text{I}_{9/2}$) and (${}^4\text{S}_{3/2}$, ${}^4\text{I}_{15/2} \rightarrow {}^4\text{I}_{9/2}$, ${}^4\text{I}_{13/2}$) cross-relaxation channels, labeled as I and II in Fig. 5. The first channel involves two nearby interacting Er^{3+} ions, one excited at the ${}^4\text{S}_{3/2}$ emitting level and the other one at the ${}^4\text{I}_{15/2}$ ground state. The first Er^{3+} ion (the donor of energy) de-excites to the ${}^4\text{I}_{13/2}$ first excited multiplet and transfers non-radiatively the energy of the transition to the other Er^{3+} ion (the acceptor of energy) that promotes from the ${}^4\text{I}_{15/2}$ ground state to the ${}^4\text{I}_{9/2}$ level. The second channel takes place between different levels, but the point is that both channels finally feed the ${}^4\text{I}_{11/2}$ level, after a fast non-radiative relaxation from the ${}^4\text{I}_{9/2}$ level and the ${}^4\text{I}_{13/2}$ lowest emitting level, which further increases their luminescence.

Assuming the intrinsic lifetime τ_0 is equal to the effective lifetime measured for the YGG1Er sample, *i.e.* considering that the energy transfer probability can be ignored, the Er^{3+} – Er^{3+} rate of energy transfer W_{ET} of the green emitting levels can be estimated for the higher Er^{3+} concentrations using eqn (2). $W_{\text{ET}} = 12\,200\text{ s}^{-1}$ for the YGG5Er and $W_{\text{ET}} = 90\,000\text{ s}^{-1}$ for the YGG10Er nano-garnets, which are comparable or much higher than the intrinsic (radiative plus multiphonon) probability of $10\,000\text{ s}^{-1}$ obtained for the ${}^2\text{H}_{11/2}$ and ${}^4\text{S}_{3/2}$ thermalized levels of the Er^{3+} ions. This rough estimation allows the conclusion that the energy transfer probability starts to be quite important in the quenching of the green luminescence for concentrations of around 5 mol% of Er^{3+} ions. The competition between the spontaneous radiative de-excitation and the cross-relaxation processes gives rise to an effective decrease in the luminescence of the ${}^2\text{H}_{11/2}$ and ${}^4\text{S}_{3/2}$ thermalized levels that, analyzing the area under the luminescence decay curves, can be estimated to be

around 65% for the YGG5Er, reaching around 90% for the YGG10Er nano-garnet.

On the other hand, the luminescence decay curves of the ${}^4\text{F}_{9/2}$ level for the three samples are quasi-exponential, as shown in the inset of Fig. 7 for the low-doped sample, and have a similar dynamics that gives the same effective lifetime of around 9.6 μs for all the Er^{3+} concentrations studied. This result is quite surprising and indicates that no efficient energy transfer process involves any Er^{3+} ion in this level; *i.e.*, no resonant or quasi-resonant cross-relaxation channels exist involving the Er^{3+} ions in the ${}^4\text{F}_{9/2}$ multiplet and, hence, no quenching of the red luminescence is observed in the YGG nano-garnets. On the contrary, the quenching of the luminescence from the ${}^4\text{I}_{9/2}$ is rather efficient, since no luminescence was measured even at low Er^{3+} concentrations. This behavior can be associated with low radiative probabilities, high multiphonon relaxation probabilities and the existence of different cross-relaxation channels, being the resonant ones, namely the (${}^4\text{I}_{9/2}$, ${}^4\text{I}_{9/2} \rightarrow {}^4\text{I}_{13/2}$, ${}^4\text{S}_{3/2}$), (${}^4\text{I}_{9/2}$, ${}^4\text{I}_{11/2} \rightarrow {}^4\text{I}_{13/2}$, ${}^4\text{F}_{9/2}$) and (${}^4\text{I}_{9/2}$, ${}^4\text{I}_{9/2} \rightarrow {}^4\text{I}_{11/2}$, ${}^4\text{F}_{9/2}$) channels labeled as III, IV and V in Fig. 5.

The luminescence decay curve of the ${}^4\text{I}_{11/2} \rightarrow {}^4\text{I}_{15/2}$ emission obtained under a 970 nm resonant laser excitation is particularly interesting since it shows a non-exponential character even for the lowest Er^{3+} concentration. Thus the energy transfer processes are also rather efficient for Er^{3+} ions in this level, due to the (${}^4\text{I}_{11/2}$, ${}^4\text{I}_{11/2} \rightarrow {}^4\text{I}_{15/2}$, ${}^2\text{H}_{11/2}$) and (${}^4\text{I}_{11/2}$, ${}^4\text{I}_{13/2} \rightarrow {}^4\text{F}_{9/2}$, ${}^4\text{I}_{15/2}$) resonant cross-relaxation channels, labeled as VI and VIII in Fig. 5, and, most probably, to quenching traps.

The luminescence decay curves of the ${}^4\text{I}_{13/2} \rightarrow {}^4\text{I}_{15/2}$ transition for all the Er^{3+} ion concentrations are single exponential, pointing to diffusion mechanisms of energy transfer.^{43,44} From the decay curves, lifetimes of the ${}^4\text{I}_{13/2}$ level have been determined by single exponential fits and found to be around 5.75, 3.25 and 1.85 ms for the YGG1Er, YGG5Er and YGG10Er nano-garnets, respectively. The variation of the lifetime of ${}^4\text{I}_{13/2}$ level with the Er^{3+} concentration is shown in the inset of Fig. 6, where it is observed that the lifetimes are decreasing monotonically with the increase of the Er^{3+} ion concentration. This effect can be associated either with the (${}^4\text{I}_{13/2}$, ${}^4\text{I}_{13/2} \rightarrow {}^4\text{I}_{15/2}$, ${}^4\text{I}_{9/2}$) resonant cross-relaxation channel, labeled as VII in Fig. 5, or, most probably, with energy transfer from Er^{3+} ions to the quenching traps.

C.3 IR-to-visible energy frequency upconversion

The phenomenon of energy upconversion in RE^{3+} -doped matrices involves different mechanisms that, after the absorption of low-energy photons, give rise to an emission of higher energy photons. It is a two-step or multi-step non-radiative process in which the main feature is the existence of at least one metastable intermediate state, which acts as a reservoir for the optically active ions, and at least one excited level at higher energy from which the RE^{3+} ions finally return to the ground state after emitting photons. The RE^{3+} ions have shown an important capability to obtain upconverted luminescence in many matrices, including oxide and fluoride ones, with important applications in optical devices such as upconverted visible laser, optical amplifiers or white light displays.¹⁰

Two possible mechanisms can be responsible for the population of the excited emitting level: the excited state absorption

(ESA) and the energy transfer upconversion (ETU). The former involves only one optically active ion successively promoted to the upper levels by the resonant absorption of two or more laser photons, whereas the latter is a many-body mechanism involving two or more nearby interacting optically active ions. Both mechanisms are not mutually exclusive and can coexist to effectively contribute to the population of the excited emitting level, although usually one of them dominates the upconversion process.^{2,14,45}

The IR-to-visible upconversion luminescence has been measured at RT by exciting the YGG1Er, YGG5Er and YGG10Er nano-garnets under 790 nm cw laser excitation in the same experimental conditions. As usual in these kinds of non-linear optical phenomena, the obtained high-energy visible emissions are visible to the naked eye. The emissions observed after exciting with a laser pump power of around 770 mW, and presented in Fig. 8, consist of two distinct bands, the first one with peaks ranging from 515 to 570 nm gives green light and is ascribed to the $(^2H_{11/2}, ^4S_{3/2}) \rightarrow ^4I_{15/2}$ transitions, whereas the second one shows red emission peaks between 645 and 680 nm associated with the $^4F_{9/2} \rightarrow ^4I_{15/2}$ transition. The upconversion spectra of the YGGEr nano-garnets are similar to those of the LuGG and GGG garnets doped with similar Er^{3+} ion concentrations.^{3,5}

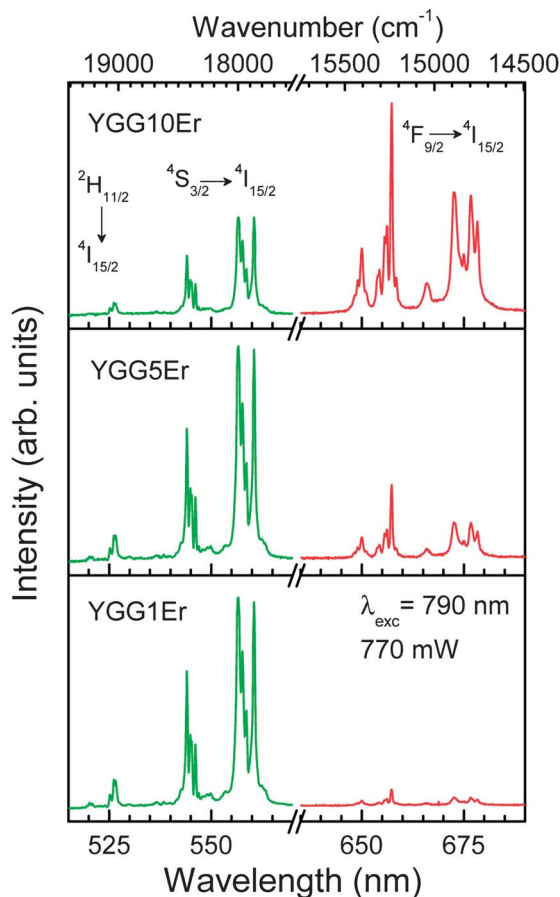


Fig. 8 NIR to green and red upconverted luminescence of the Er^{3+} ions in YGG1Er, YGG5Er and YGG10Er nano-garnets after a 790 nm cw laser excitation resonantly with the $^4I_{15/2} \rightarrow ^4I_{9/2}$ transition at RT for a pump power of 770 mW.

It is worth noting that the main feature observed when comparing the upconverted luminescences for the three nano-garnets under study is that the relative intensities of the green and red upconverted emissions strongly depend on the Er^{3+} concentration, as can be observed in Fig. 8. This feature opens the possibility of a tunability of the upconverted luminescence that can be exploited in different optical devices.

The green-to-red intensity ratio obtained for the YGG1Er is around 10, quite similar to that obtained under blue laser excitation. However, this ratio decreases almost to 3 for the YGG5Er nano-garnet, slightly but significantly smaller than in the Stokes experiments, and it dramatically falls to around 0.4 for the YGG10Er with the highest doping concentration of Er^{3+} ions, which is a factor 5 times smaller when exciting with the blue laser rather than with the IR laser. These differences are due to the non-linear character of the upconversion processes and the presence of new and concentration-dependent mechanisms that populate the $^4F_{9/2}$ red emitting level more efficiently, as will be shown later.

A first step in the analysis of the mechanisms involved in the IR-to-visible upconversion process is the measurement of the dependence of the upconverted emission intensities on the IR laser pump power for the three nano-garnets under study. It is known that the upconversion intensity I_{UC} will be proportional to a power n of the IR excitation intensity I_{IR} ; i.e., $I_{UC} \propto (I_{IR})^n$, where n is the number of IR photons absorbed per visible photon emitted.⁴⁶ The evaluated values for n are 2.05, 1.69, and 1.57 for green emissions and 1.92, 1.65 and 1.46 for red emissions for the YGG1Er, YGG5Er and YGG10Er nano-garnets, respectively (see Fig. 9). The nearly quadratic dependency observed for all the intensities with the laser pump power indicates that two quanta of energy equivalent to two 790 nm IR photons are involved in the population of the $^2H_{11/2}$, $^4S_{3/2}$, and $^4F_{9/2}$ emitting levels, by either a two-photon ESA or by two- Er^{3+} ETU mechanisms. Although a strictly quadratic dependence may be expected, an experimentally observed decrease in the slopes of the upconverted emission intensities *versus* pump power may occur, reaching a linear dependency in the limit of infinitely large upconversion rates.⁴⁶

An easy way to distinguish which is the main mechanism responsible for the upconversion processes is through the measurement of the dynamics of the upconversion luminescence after a 790 nm laser pulsed excitation, and their comparison with the temporal evolution of the Stokes emission exciting resonantly at each level. For this purpose the temporal evolution of green upconverted emissions has been measured for all Er^{3+} -doped nano-garnets, exciting with a 790 nm pulsed OPO laser, and is shown in Fig. 10 (black curves). The curves of all nano-garnets have been compared with the luminescence decay curves (see green curves in Fig. 10) obtained under blue laser excitation, with an energy resonant with the $^4I_{15/2} \rightarrow ^4F_{7/2}$ transition, after which the Er^{3+} ions immediately relax to the green emitting thermalized levels. Different dynamics are observed for the three nano-garnets studied, indicating different degrees of mixing between the ESA and ETU mechanisms depending on the Er^{3+} concentrations.

As already mentioned, the ESA and ETU mechanisms may coexist to effectively contribute to the population of the excited emitting level, although usually one of them dominates the

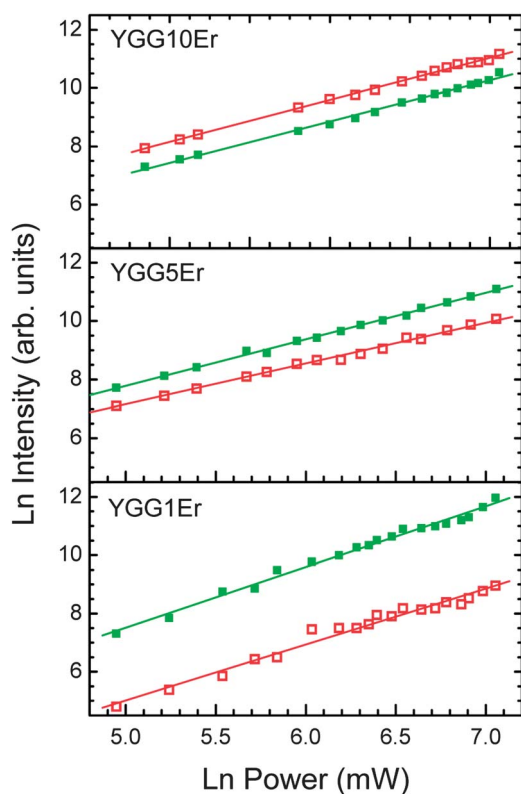


Fig. 9 Dependence of the green (closed symbol) and the red (open symbol) upconverted emission intensities of the Er^{3+} ions in YGG1Er, YGG5Er and YGG10Er nano-garnets with the laser pump power at RT.

upconversion process. In the case of ESA, when the nano-garnet is excited with the 790 nm laser pulse, the Er^{3+} ions in the ground state reach the intermediate $^4\text{I}_{9/2}$ level through a ground state absorption (GSA) process and, during the same laser pulse, absorb a second IR photon to promote to the high energy levels, a mechanism labelled as ESA1 in Fig. 11. However, since $^4\text{I}_{9/2}$ cannot be considered a metastable level, it is more probable that the Er^{3+} ions immediately relax non-radiatively to the $^4\text{I}_{11/2}$ and the $^4\text{I}_{13/2}$ levels, typically in the femtosecond range, before absorbing the second laser photon. In this process they follow the resonant channels labelled as ESA2 and ESA3, to reach the $^4\text{F}_{3/2}$ and the $^2\text{H}_{11/2}$ levels, respectively, which finally result in population of both $^2\text{H}_{11/2}$ and $^4\text{S}_{3/2}$ thermalized green emitting levels. Of these two excited state absorption mechanisms, ESA3 is more probable due to the longer lifetime of the $^4\text{I}_{13/2}$ level, although the efficiency of the ESA mechanism lies also in the resonance of the absorption processes, one from the ground state to the intermediate level and a second one from this level to the emitting one. In any of these cases, and as a fingerprint of this mechanism, the temporal evolution of the green upconverted emission from the emitting level, and hence its lifetime, after the laser pulse following an ESA mechanism should be exactly the same as that obtained by exciting this level resonantly through a pure ground state absorption (GSA).

On the other hand, if the ETU mechanism dominates the upconversion process, one or different energy transfer processes could take place between nearby Er^{3+} ions in the ground and in the intermediate $^4\text{I}_{11/2}$ and $^4\text{I}_{13/2}$ states. The most resonant

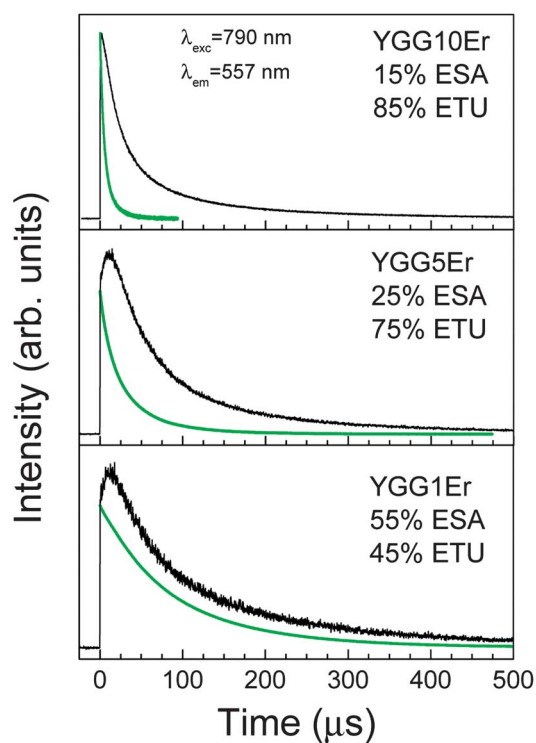


Fig. 10 Temporal evolution of the green upconverted luminescence of the Er^{3+} ions in YGG1Er, YGG5Er and YGG10Er nano-garnets after a 790 nm laser pulsed excitation. The luminescence decay curves of the green emission under direct excitation of the $^2\text{H}_{11/2}$ and $^4\text{S}_{3/2}$ multiplets at 525 nm are also included for comparison.

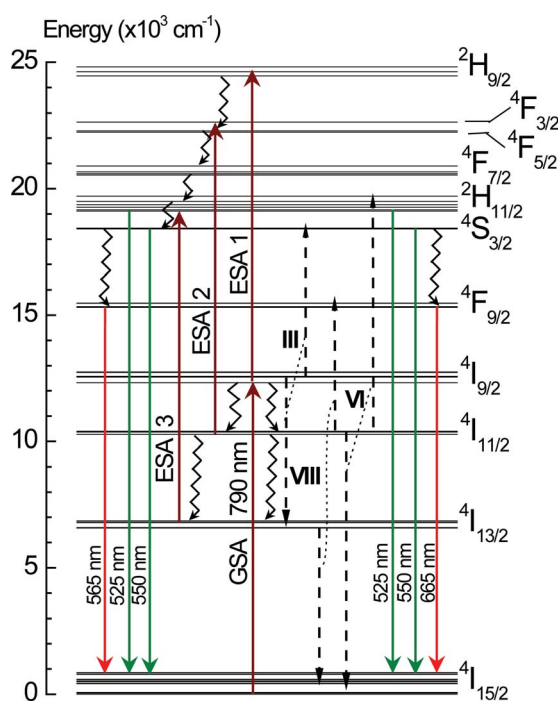


Fig. 11 Partial energy level structure of Er^{3+} ions showing the different radiative (downward solid lines), multiphonon (zig-zag lines), excited state absorption (ESA, upward solid lines) and energy transfer (roman numbers) processes related to the green and red upconverted emissions under a 790 nm laser excitation.

cross-relaxation channels involving these intermediate levels, as well as the $^4I_{9/2}$ level, are presented in Fig. 11 labelled as III and VI, as discussed in the previous section. This non-radiative interaction also depends strongly on the inter-ionic distances between the optically active ions and starts after the laser pulse, needing some time to promote the Er^{3+} ions to the emitting level. Thus there is an initial rise in the temporal evolution of the emission intensity after the laser pulse. The efficiency of this mechanism depends on the concentration of Er^{3+} ions and the resonance between the emission and absorption profiles of the transitions involved.

The temporal evolution of the upconverted green luminescence in the YGG nano-garnet, shown in Fig. 10, has an initial rise from the non-zero population of the emitting state followed by a slow decrease in the population. The non-zero population of the thermalized levels is the fingerprint of the ESA processes while the following rise indicates that a second mechanism is feeding the emitting levels through ETU mechanisms. Since the lifetimes of the intermediate levels are involved in the process, the intensity of the upconverted emission reaches its maximum at around 10 μs after the laser pulse for the YGG1Er. This delay is quite similar for the YGG5Er and it decreases to 1.5 μs for the YGG10Er, being almost negligible due to the highly efficient energy transfer processes involving the de-excitation of the thermalized levels. In order to obtain quantitative values of the percentage of ESA and ETU mechanisms in the green upconverted emission, the Stokes luminescence decay curve of the emitting level under resonant excitation, with an initial value that equals the value of the non-zero initial value at $t = 0$, is superimposed on the temporal evolution of the intensity of the upconverted emission after a laser pulsed at 790 nm at RT.⁴⁷ Comparing the area under the temporal evolution of the Stokes luminescence with the total area, it can be concluded that the ESA and the ETU mechanisms share the responsibility of the upconverted green luminescence of the YGG1Er nano-garnets with nearly 50% for each mechanism. In the case of the YGG5Er and YGG10Er nano-garnets, the ETU is the dominant mechanism with a percentage that increases with the Er^{3+} concentration (see Fig. 10).

With regards to the $^4F_{9/2} \rightarrow ^4I_{15/2}$ red upconverted emission, there is one relevant point to consider that has been commented on previously; an increase of the red emission compared to the green one that is much larger compared with the relative intensities obtained from 488 nm direct laser excitation and that is directly dependent on the Er^{3+} concentration. This should indicate different natures in the non-linear mechanisms involved for each level.⁴¹ In order to analyze the mechanisms involved in the upconversion process for the red emission, its temporal evolutions under a 790 nm laser pulse for the nano-garnets studied are shown in Fig. 12 (black curves), together with the temporal evolution of the red emission exciting resonantly at 525 nm the $^2H_{11/2}$ and $^4S_{3/2}$ thermalized levels (green curves) and at 655 nm the $^4F_{9/2}$ level (red curves).

None of the upconverted luminescence dynamics for the YGG nano-garnets studied follow a pure exponential behavior, contrary to the red emission after a resonant excitation into the $^4F_{9/2}$ level (see Fig. 7 and 12), making the dynamics of this level quite complex. Moreover, from Fig. 11 it can be observed that none of the ESA mechanisms that can be induced after a 790 nm

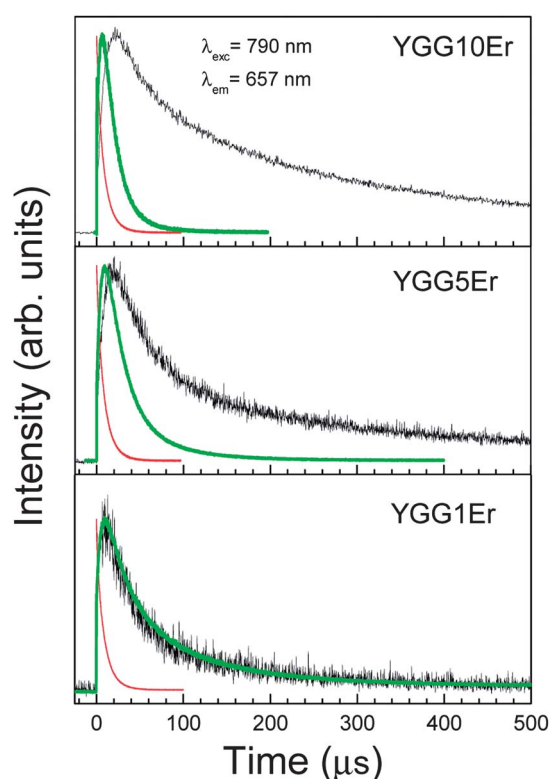


Fig. 12 Temporal evolution of the red upconverted luminescence of the Er^{3+} ions in YGG1Er, YGG5Er and YGG10Er nano-garnets after a 790 nm pulsed excitation. The luminescence decay curves of the red emission under direct excitation of the $^4F_{9/2}$ level at 655 nm (thin line) and exciting at 525 nm the $^4I_{15/2} \rightarrow ^2H_{11/2}$ transition (thick line) are also included for comparison.

laser excitation can be used to resonantly feed the $^4F_{9/2}$ level from which the red emission takes place. From the dynamics of the red upconverted emissions of the YGG1Er nano-garnet obtained exciting at 790 nm and at 525 nm resonantly with the $^2H_{11/2}$ level, it can be concluded that, for such a relatively low Er^{3+} concentration, the $^4F_{9/2}$ is populated through radiative and multiphonon relaxation from the $^2H_{11/2}$ and $^4S_{3/2}$ thermalized levels. For higher Er^{3+} concentrations, the longer temporal evolutions reveal the presence of a different energy transfer mechanisms that feed the red emitting level. Thus the only way to populate this level after a 790 nm laser excitation is from the thermalized $^2H_{11/2}$ and $^4S_{3/2}$ levels, populated using the above-mentioned mechanisms, and through an efficient, resonant energy transfer cross-relaxation mechanism labeled as VIII in Fig. 5 and 11, in which the $^4I_{11/2}$ and the $^4I_{13/2}$ levels act as reservoir metastable levels. Taking into account that the lifetime of the $^4F_{9/2}$ level is independent of the Er^{3+} concentration, the long lifetimes of these metastable levels even at such high concentrations as that in the YGG10Er nano-garnet confirm the existence of cross-relaxation channels that feeds the red emitting level.

The enhancement of the red emission with respect to the green one as a function of the Er^{3+} concentration indicates that the ETU mechanism, which populates the $^4F_{9/2}$ level, is more effective than those corresponding to the $^2H_{11/2}$ and $^4S_{3/2}$ thermalized levels. Thus a tunability of the intensities of the combined green

and red upconverted emissions is possible in the Er³⁺-doped YGG nano-garnets.

D Conclusions

The synthesis of Er³⁺-doped Y₃Ga₅O₁₂ (YGG) nanocrystals has been successfully carried out *via* a citrate sol–gel synthesis. X-ray diffraction measurements confirm that the nanocrystals are formed in a single phase of the garnet structure with an average grain size of 60 nm, whereas HRTEM pictures show that the nanoparticles are agglomerated in interconnected spherical and elliptical shapes. The vibrational properties of the YGG nano-garnets determined by Raman and FTIR spectroscopy also confirm the good crystalline nature of the single phase nanoparticles and show that several impurities are attached to the nanocrystal surface. The peaks observed in the absorption and luminescence spectra are due to the incorporation of the Er³⁺ ions into the low-phonon energy dodecahedral site, replacing the Y³⁺ position, since the interaction of the Er³⁺ ions with the oxygen ligands in a D₂ local point symmetry completely breaks the degeneracy of the free-Er³⁺ multiplets. When exciting the Er³⁺ ions in the blue range, intense green, red and infrared emissions are observed, starting from four emitting levels, whose intensities strongly depend on the Er³⁺ concentration. Different luminescence dynamics observed for the different emitting levels for the higher doped nano-garnets indicate the presence of different cross-relaxation mechanisms between Er³⁺ ions and the transfer of energy to quenching traps. The red-to-green intensity ratios increase due to cross-relaxation channels that efficiently quench the radiative de-excitation of the ²H_{11/2}, ⁴S_{3/2} green emitting levels, whereas that of the ⁴I_{9/2} red emitting level is not affected. Under cw 790 nm laser excitation the Er³⁺-doped YGG nano-garnets show bright and intense green and red upconverted luminescence. Different dynamics are observed for the green and red upconverted emissions. Both ESA and ETU mechanisms are involved in the upconverted green luminescence of the YGG1Er nano-garnets with nearly 50% for each mechanism, whereas ETU is dominant in the upconverted green luminescence of the YGG5Er and YGG10Er nano-garnets. The enhancement of the red emission with respect to the green one for the high-doped nano-garnets is ascribed to the existence of cross-relaxation channels activated by the infrared laser. This ETU mechanism populates the ⁴F_{9/2} level more efficiently than those corresponding to the ²H_{11/2} and ⁴S_{3/2} thermalized levels. These results indicate that a tunability of the intensities of the combined green and red upconverted emissions is possible in the Er³⁺-doped YGG nano-garnets, making the YGG nano-garnet a potential and interesting material in different optical devices such as in two-dimensional displays or upconversion lasers.

Acknowledgements

This work has been partially supported by Ministerio de Ciencia e Innovación of Spain (MICCIN) under The National Program of Materials (MAT2010-21270-C04-02; -03; -04), The Consolidator-Ingenio 2010 Program (MALTA CSD2007-0045), and The National Infrastructure Program, by Ministerio de Economía y Competitividad of Spain (MINECO) within The Indo-Spanish Joint Programme of Cooperation in Science and

Technology (PRI-PIBIN-2011-1153/DST-INT-Spain-P-38-11), and by the EU-FEDER funds (UCAN08-4E-008). S.F. León-Luis and V. Monteseuro wish to thank MICINN for the FPI grants (BES-2008-003353 and BES-2011-044596). Dr V. Venkatramu is grateful to DAE-BRNS, Government of India for the award of DAE Research Award for Young Scientists (no. 2010/20/34/5/BRNS/2223).

Notes and references

- 1 A. Speghini, F. Piccinelli and M. Bettinelli, *Opt. Mater.*, 2011, **33**, 247.
- 2 F. Wang and X. Liu, *Chem. Soc. Rev.*, 2009, **38**, 976.
- 3 V. Venkatramu, D. Falcomer, A. Speghini, M. Bettinelli and C. K. Jayasankar, *J. Lumin.*, 2008, **128**, 811.
- 4 V. Venkatramu, M. Giarola, G. Mariotto, S. Enzo, S. Polizzi, C. K. Jayasankar, F. Piccinelli, M. Bettinelli and A. Speghini, *Nanotechnology*, 2010, **21**, 175703.
- 5 F. Vetrone, J. C. Boyer, J. A. Capobianco, A. Speghini and M. Bettinelli, *J. Phys. Chem. B*, 2003, **107**, 1107.
- 6 D. Hreniak, W. Strek, P. Gluchowski, M. Bettinelli and A. Speghini, *Appl. Phys. B: Lasers Opt.*, 2008, **91**, 89.
- 7 E. Caponetti, D. C. Martino, M. L. Saladino and C. Leonelli, *Langmuir*, 2007, **23**, 3947.
- 8 R. Krsmanovic, V. A. Morozov, O. I. Lebedev, S. Polizzi, A. Speghini, M. Bettinelli and G. Van Tendeloo, *Nanotechnology*, 2007, **18**, 325604.
- 9 R. Naccache, F. Vetrone, A. Speghini, M. Bettinelli and J. A. Capobianco, *J. Phys. Chem. C*, 2008, **112**, 7750.
- 10 F. Auzel, *Chem. Rev.*, 2004, **104**, 139.
- 11 G. L. Vossler, C. L. Brooks and K. A. Winik, *Electron. Lett.*, 1995, **31**, 1162.
- 12 T. H. Whitley, C. A. Millar, R. Wyatt, M. C. Brierley and D. Szebesta, *Electron. Lett.*, 1991, **27**, 1785.
- 13 J. E. Roman, P. Camy, M. Hempstead, W. S. Brocklesby, S. Nouth, A. Beguin, C. Lermiaux and J. S. Wilkinson, *Electron. Lett.*, 1995, **31**, 1345.
- 14 A. Pollack and D. B. Chang, *J. Appl. Phys.*, 1988, **64**, 2885.
- 15 L. H. Spangler, B. Farris, E. D. Filer and N. P. Bames, *J. Appl. Phys.*, 1996, **79**, 573.
- 16 V. Mahalingam, F. Mangiarini, F. Vetrone, V. Venkatramu, M. Bettinelli, A. Speghini and J. A. Capobianco, *J. Phys. Chem. C*, 2008, **112**, 17745.
- 17 G. H. Dieke and H. M. Crosswhite, *Appl. Opt.*, 1963, **2**, 675.
- 18 S. Sanders, R. G. Waarts, D. G. Mehuys and D. F. Welch, *Appl. Phys. Lett.*, 1995, **67**, 1815.
- 19 F. Hanson, *Appl. Phys. Lett.*, 1995, **66**, 3549.
- 20 P. E.-A. Möbert, E. Heumann, G. Huber and B. H. T. Chai, *Appl. Phys. Lett.*, 1998, **73**, 139.
- 21 F. Yu, D. Yuan, X. Cheng, X. Duan, X. Wang, L. Kong, L. Wang and Z. Li, *Mater. Lett.*, 2007, **61**, 2322.
- 22 Y. X. Pan, M. Wu and Q. Su, *Mater. Sci. Eng., B*, 2004, **106**, 251.
- 23 A. Katelnikovas and A. Kareiva, *Mater. Lett.*, 2008, **62**, 1655.
- 24 H. M. Rietveld, *J. Appl. Crystallogr.*, 1969, **2**, 65.
- 25 J. Rodriguez-Carvajal, *Phys. Rev. B: Condens. Matter Mater. Phys.*, 1993, **192**, 55.
- 26 N. Matsushita, N. Tsuchiya, K. Kanatsuka and T. Yanagitani, *J. Am. Ceram. Soc.*, 1999, **82**, 1977.
- 27 F. Euler and J. A. Bruce, *Acta Crystallogr.*, 1965, **19**, 971.
- 28 K. Binnemans and C. J. Görller-Walrand, *Phys. Rev. B: Condens. Matter Mater. Phys.*, 1997, **9**, 1637.
- 29 K. Papagelis, J. Arvanitidis, E. Vinga, D. Christofilos, G. A. Kourouklis, H. Kimura and S. Ves, *J. Appl. Phys.*, 2010, **107**, 113504.
- 30 A. Leleckaite and A. Kareiva, *Opt. Mater.*, 2004, **26**, 123.
- 31 J. P. Hurrell, S. P. S. Porto, I. F. Chang, S. S. Mitra and R. P. Bauman, *Phys. Rev.*, 1958, **173**, 851.
- 32 R. L. Wadsack, J. L. Lewis, B. E. Argyle and B. K. Chang, *Phys. Rev. B: Solid State*, 1971, **3**, 4342.
- 33 J. J. Song, P. B. Klein, R. L. Wadsack, M. Selders, S. Mroczkowski and R. K. Chang, *J. Opt. Soc. Am.*, 1973, **63**, 1135.
- 34 M. C. Saine, E. Husson and H. Brusset, *Spectrochim. Acta, Part A*, 1982, **38**, 25.

- 35 K. Papagelis, G. Kanellis, S. Ves and G. A. Kourouklis, *Phys. Status Solidi B*, 2002, **233**, 134.
- 36 B. G. Wybourne, *Spectroscopic Properties of Rare Earths*, Wiley-Interscience, 1965.
- 37 M. J. Weber, *Phys. Rev.*, 1967, **157**, 262.
- 38 G. H. Dieke, *Spectra and Energy Levels of Rare-Earth Ions in Crystals*, Wiley-Interscience, 1968.
- 39 C. A. Morrison and R. P. Leavitt, *Handbook on the Physics and Chemistry of Rare Earths*, ed. K. A. Gschneidner Jr and L. Eyring, Elsevier, Amsterdam, 1982, 5, 461.
- 40 P. Dorenbos, *J. Lumin.*, 2000, **91**, 91.
- 41 X. Chen, T. Nguyen, Q. Luu and B. Di Bartolo, *J. Lumin.*, 2000, **85**, 295.
- 42 B. Di Bartolo, *Energy transfer among ions in solids in Energy Transfer in Condensed Matter*, ed. B. Di Bartolo, NATO ASI Series, Plenum Press, 1984, vol. 114.
- 43 F. Auzel, F. Bonfigli, S. Gagliari and G. Baldacchini, *J. Lumin.*, 2001, **94–95**, 293.
- 44 F. Auzel, G. Baldacchini, L. Laversenne and G. Boulon, *Opt. Mater.*, 2003, **24**, 103.
- 45 J. Fernández, R. Balda, A. Mendioroz, M. Sanz and J.-L. Adam, *J. Non-Cryst. Solids*, 2001, **287**, 437.
- 46 M. Pollnau, D. R. Gamelin, S. R. Lüthi, H. U. Güdel and M. P. Hehlen, *Phys. Rev. B: Condens. Matter*, 2000, **61**, 3337.
- 47 R. Valiente, O. S. Wenger and H. U. Güdel, *J. Chem. Phys.*, 2002, **116**, 5196.